Electronic Supplementary Material (ESI) for Energy & Environmental Science.

Enhanced oxygen exchange of perovskite oxide surfaces through strain-driven chemical stabilization

Bonjae Koo, ‡[a] Hyunguk Kwon, ‡[b] YeonJu Kim,[a] Han Gil Seo,[a] Jeong Woo Han*[b] and WooChul Jung*[a]

[a] *Department of Materials Science and Engineering, Korea Advanced Institute of Science and Technology (KAIST), Daejeon, Republic of Korea*

[b] *Department of Chemical Engineering, University of Seoul (UOS), Seoul, Republic of Korea*

‡ *Authors contributed equally to this work. * to whom correspondence should be addressed.*

Supplementary Figure & Table

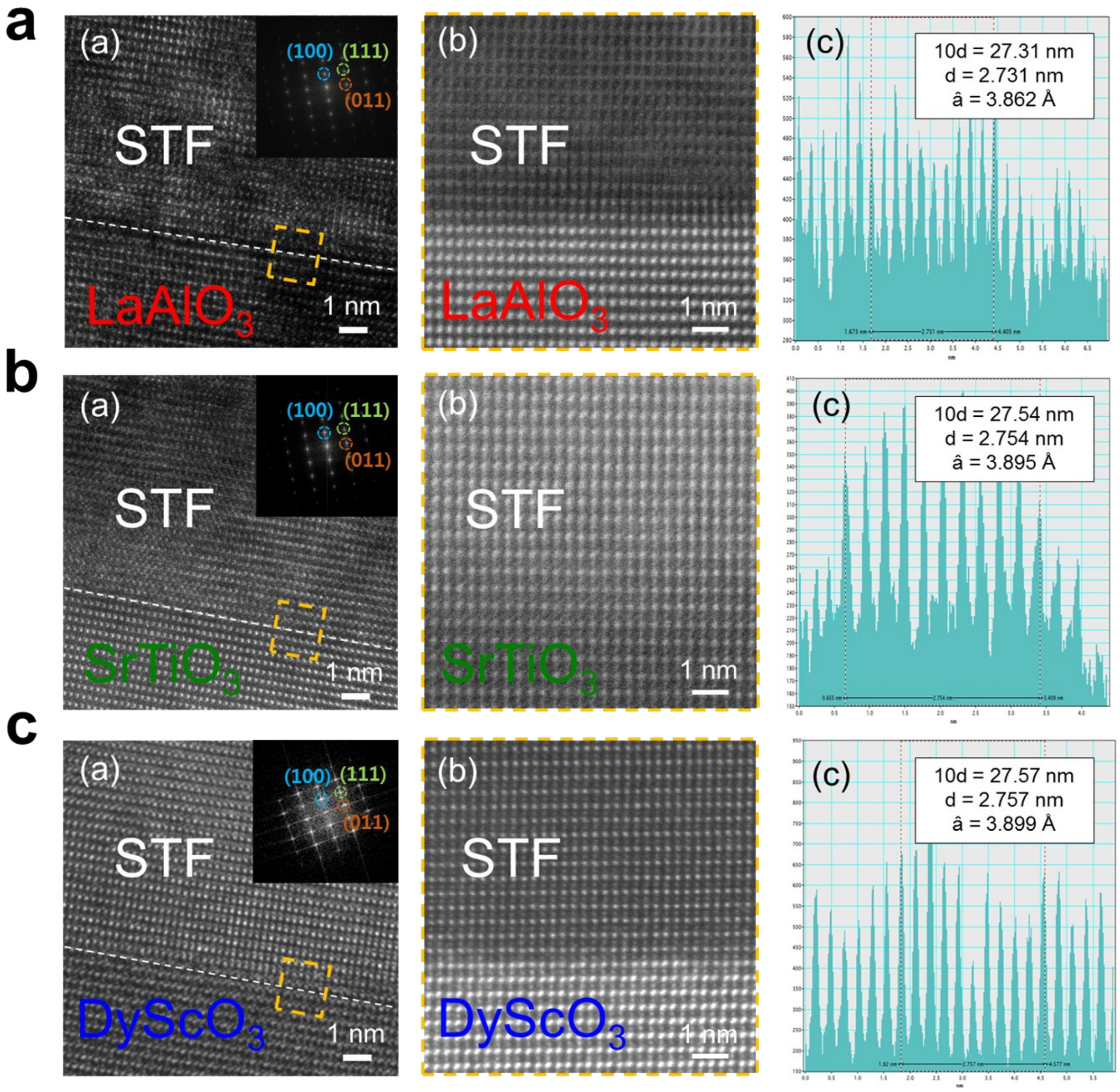

Figure S1| **a**, (a) High resolution transmission electron microscopy (HR-TEM), fast Fourier transform (FFT), (b) scanning transmission electron microscopy (STEM) images, and (c) a line scanning profile showing the average distance between 10 atoms of epitaxial $SrTi_{0.5}Fe_{0.5}O_{3-\delta}$ (STF) thin films on single-crystal $LaAlO_3$ **b**, $SrTiO_3$ and **c,** $DyScO_3$ substrates, respectively.

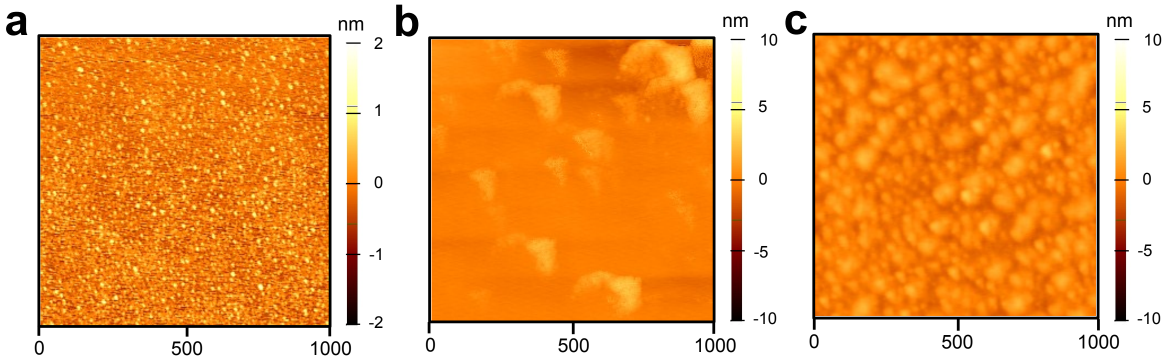

Figure S2| **a**, Atomic force microscopy (AFM) micrographs of epitaxial $SrTi_{0.5}Fe_{0.5}O_{3-\delta}$ (STF) thin films on single-crystal $LaAlO_3$, **b**, $SrTiO_3$ and **c**, $DyScO_3$ substrates, respectively.

Table S1| **a**, Calculated root-mean-square (RMS) surface roughness and actual surface area in a 1 mm x 1 mm area, as determined by AFM data analysis.

Sample	**Surf. roughness (nm)**	**Surf. area in 1 mm x 1 mm (mm^2)**
STF on LAO	0.176 ± 0.16	1.002
STF on STO	0.363 ± 0.23	1.001
STF on DSO	0.658 ± 0.10	1.002

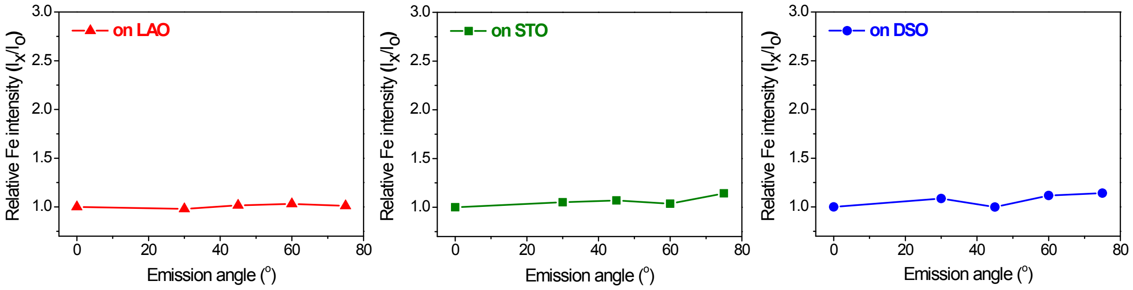

Figure S3| The relative Fe intensity of epitaxial $SrTi_{0.5}Fe_{0.5}O_{3-\delta}$ (STF) thin films on single-crystal $LaAlO_3$ (LAO), $SrTiO_3$ (STO) and $DyScO_3$ (DSO) substrates with varying emission angles (X) from bulk (θ = 0°) to surface (θ = 75°), measured by angle resolved X-ray photoelectron spectroscopy (AR-XPS).

Table S2| Sr and Fe molar fraction of a polycrystalline $SrTi_{0.5}Fe_{0.5}O_{3-\delta}$ (STF) thin film measured by inductively coupled plasma mass spectroscopy (ICP-MS) analysis.

	Sr		**Fe**	
Material	mol.%	Relative mol.%	mol.%	Relative mol.%
STF	54.0 ± 0.8	100	26.8 ± 0.5	49.6 ± 1.7

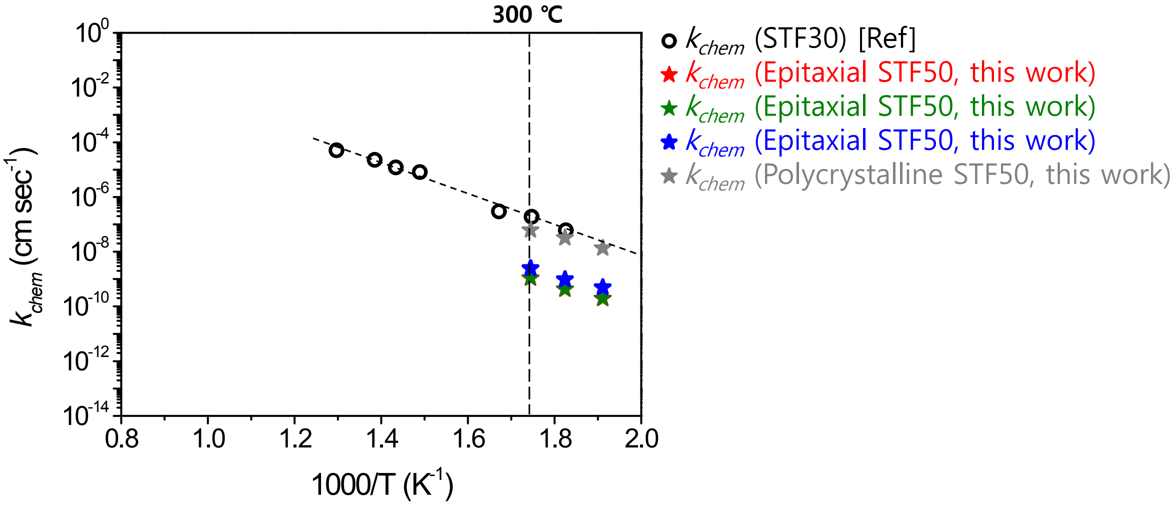

Figure S4| Arrhenius plot of the chemical exchange coefficients (k_{chem}) of $SrTi_{1-x}Fe_xO_{3-\delta}$ (STF100x) reported in this study and in the literature [Ref: R. Merkel and J. Maier, *Angew. Chem. Int. Ed.,* 2008, **47**, 3874-3894.]

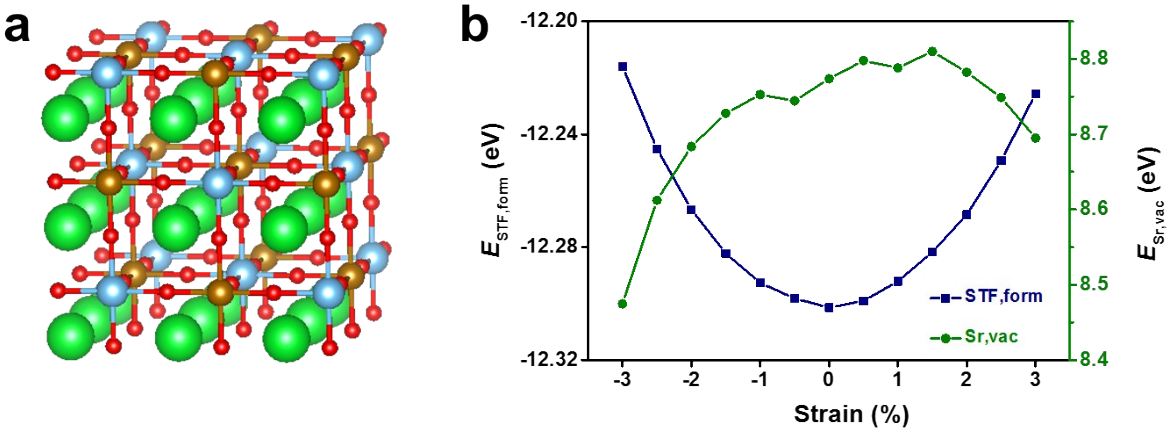

Figure S5| **a**, Unit cell of (3×3×3) SrTi$_{0.52}$Fe$_{0.48}$O$_3$ (STF48) bulk. **b**, $E_{STF,form}$ and $E_{Sr,vac}$ as functions of strain for STF48.

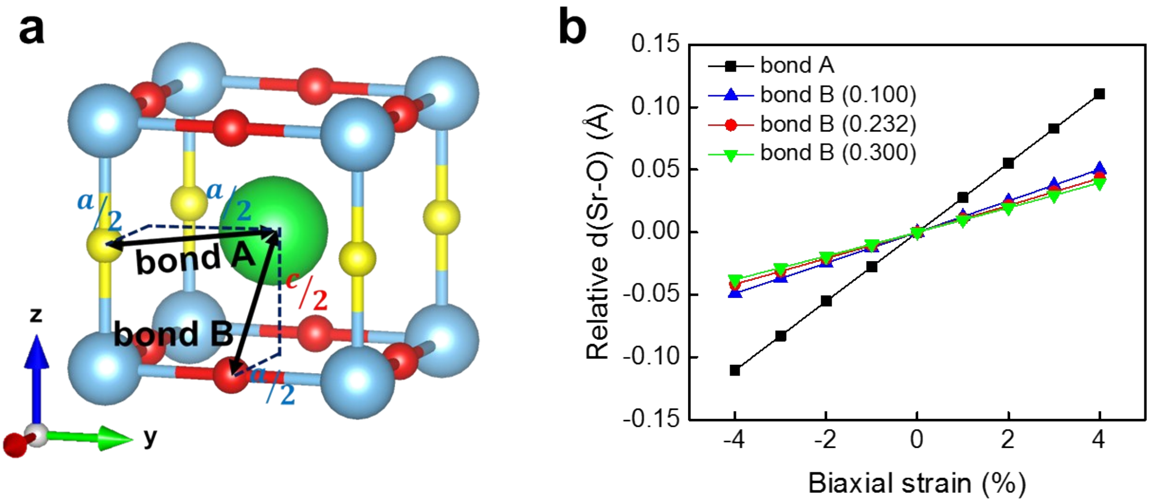

Figure S6| **a**, Two types of Sr-O bonds in the biaxially strained $SrTiO_3$ perovskite: bond A and bond B. *a* and *c* are in-plane and out-of-plane lattice constants, respectively. The Sr atom is light green, the Ti atom is cyan, the O atom in the SrO layer is yellow, and the O atom in the TiO_2 layer is red. **b**, Distances of bond A and bond B under the strain state relative to that in the strain-free equilibrium state. A lattice constant of 3.905 Å was used for the unstrained state to calculate the relative distances. The numbers in parentheses indicate the Poisson ratio used to calculate out-of-plane lattice constant.

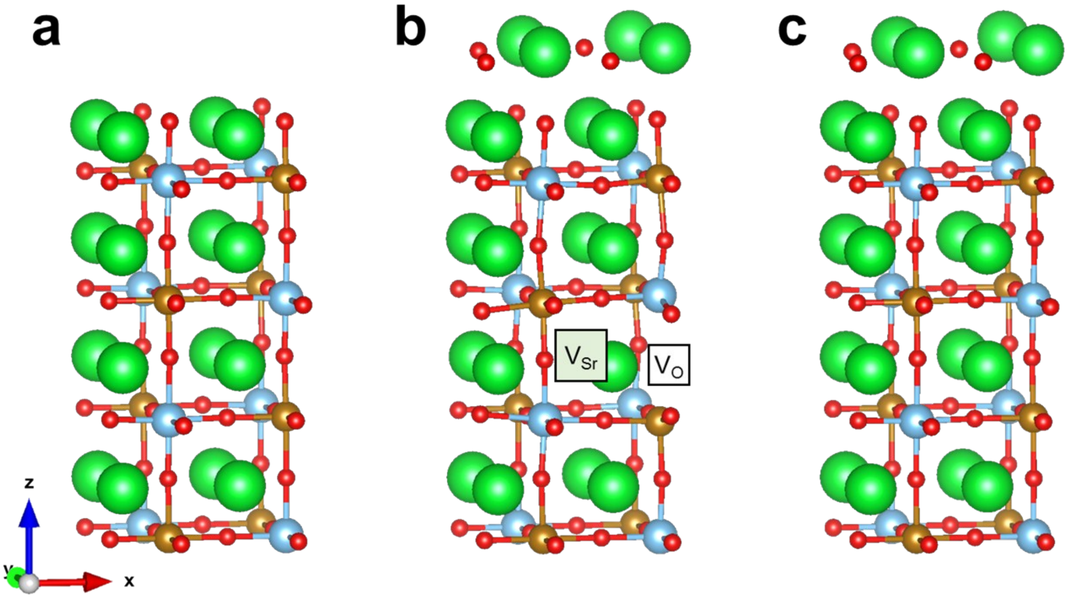

Figure S7| Unit cell of the $SrTi_{0.5}Fe_{0.5}O_3$ (STF) surface. **a**, Perfect slab model and **b**, slab model with a SrO monolayer on the topmost layer and Sr and O vacancies in the bulk layer. **c**, Slab model with a SrO monolayer on the topmost layer. Sr atom is green, Ti atom is sky blue, Fe atom is brown and O atom is red, respectively.

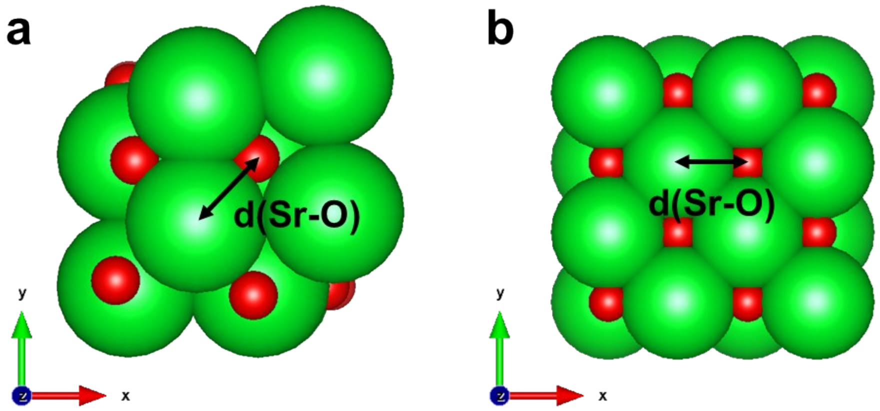

Figure S8| **a**, Top view of the $SrTi_{0.5}Fe_{0.5}O_3$ (STF) surface with a SrO monolayer. **b**, SrO bulk. The Sr-O bond length of the SrO monolayer was obtained by averaging all the Sr-O bonds within the SrO monolayer.

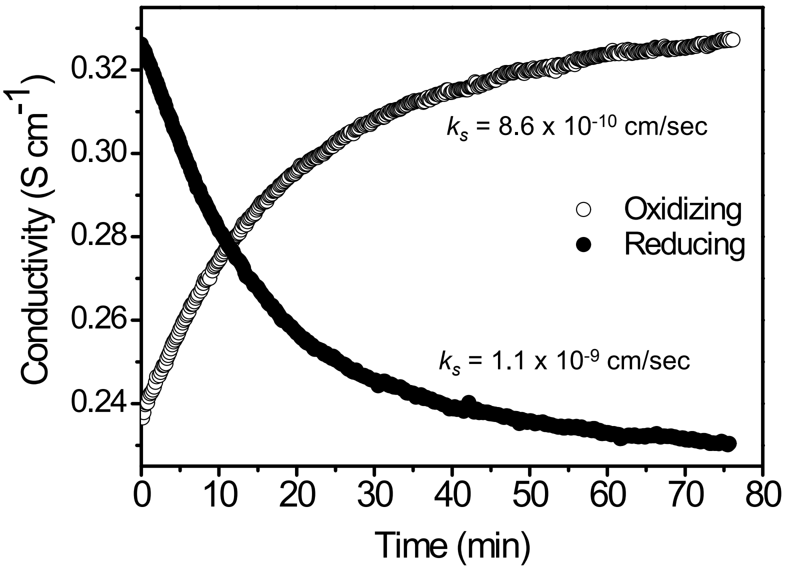

Figure S9| Raw conductivity relaxation profiles along the reducing and oxidizing directions for a pO_2 switch between 0.21 atm and 1 atm at 300˚C. The relaxation profiles are almost identical, indicating that the pO_2 change is small enough to ensure that the driving force and k_s are the same along both directions and that the system response is linear.

Experimental details

Sample preparation

$SrTi_{0.5}Fe_{0.5}O_{3-\delta}$ (STF) thin films were grown by pulsed laser deposition (PLD) from oxide targets of the respective materials and deposited onto (001)-oriented $LaAlO_3$ (LAO), $SrTiO_3$ (STO) and (110)-oriented $DyScO_3$ (DSO) single-crystal substrates (10 mm × 10 mm × 5 mm, MTI Corporation). The oxide targets were prepared by a conventional solid state reaction, starting from $SrCO_3$ (Alfa Aesar, 99.99%), TiO_2 (Alfa Aesar, 99.9%), and Fe_2O_3 (Alfa Aesar, 99.945%) powders. The powders were mixed to obtain the desired Sr:Ti:Fe stoichiometric ratios, and ball milled for 24 h with high purity ethanol (Merck, 99.9%) before drying. The well-mixed powders were then calcined in air at 1250 ^oC for 8 h with heating and cooling rates of 4 ^oC/min. Pellet-type PLD targets were prepared by uniaxial pressing followed by cold isostatic pressing at 200 MPa. The compacted green bodies were sintered at 1425 ^oC for 8 h with heating and cooling rates of 4 ^oC/min.

The PLD system (VTS Corporation) was operated with a KrF excimer laser, emitting at 248 nm (Coherent COMPex Pro 205), with an energy of 300 mJ/pulse with a repetition rate of 2 Hz. The substrates were heated to 700 ^oC during deposition, while the oxygen pressure was maintained at 5 mTorr after pumping the background pressure to 10^{-5} Torr. After deposition and prior to cooling, the oxygen pressure in the chamber was increased to approximately 1 Torr for 20 min or longer to allow the more complete oxidation of the films. The resulting films had a typical thickness of ~25 nm.

Physical and chemical characterization

High resolution X-ray diffraction (HR-XRD, X'Pert-PRO MRD, PANalytical) measurements were performed for both the in-plane and out-of-plane reflections of the deposited thin films on single-crystal LAO (001), STO (001), and DSO (110) substrates using Cu Kα radiation ($\lambda=$

1.541 Å). HR-XRD was operated at 45 kV and 40 mA with a fixed Cu anode with a hybrid monochromator including a four-bounce Ge (220) crystal and a parabolic multilayer mirror. The range of out-of-plane (2θ-ω scan) was 20° to 60° and that of in-plane (ϕ scan) was 360°. The in-plane alignment of thin films was confirmed from the (110) parallel with the substrate by the 45° tilted sample as the (111) plane of a cubic structure. The surface roughness and morphology of the samples were characterized by atomic force microscopy (AFM, NX10, Park Systems) in non-contact mode. The micrographs were analyzed to determine the root mean square (RMS) surface roughness using the XEI software. Cross-sectional high resolution transmission electron microscopy and scanning transmission electron microscopy (HR-TEM and STEM, Titan cubed G2 60-300, FEI company) was used at an acceleration voltage of 300 kV after focused ion beam (FIB, Quanta 3D FEG, FEI company) milling. Angle resolved X-ray photoelectron spectroscopy (AR-XPS, Sigma Probe, Thermo Fisher Scientific) of the surface of STF thin films was performed using monochromated Al Kα (hν = 1486.6 eV) radiation under ultrahigh vacuum with a standard detector and 4-channel detector (30°, 45°, 60° and 75°). All AR-XPS spectra were energy calibrated to the C 1s peak with a binding energy of 284.8 eV and quantitative analysis from the AR-XPS spectra was performed based on the Shirley background.

Electrical conductivity relaxation measurements

For the ECR measurements, two platinum (Pt) electrodes as current collectors (100 nm-thick and 1 mm-distance) were applied to the STF thin films by DC magnetron sputtering (with a DC power of 100 W and an Ar working pressure of 2.2 mTorr) using a metal shadow mask. The measurements were made at 300 °C in a tube furnace, and 150 sccm of N_2-based gas with 0.21 atm (=pO_2^1) and 1 atm (=pO_2^2) oxygen partial pressures was delivered separately via mass flow controllers (MFCs, Fujikin). The sample was first kept at equilibrium in pO_2^1, and the atmosphere was changed abruptly to pO_2^2 by a four-way valve at a constant temperature, while monitoring the in-plane conductivity (which reflects the change in oxygen content in the sample) at each second with an applied DC voltage of 50 mV across the length of the specimen and measuring the current via chronoamperometry (CA, VSP-300, Biologic). Both the oxidation and reduction rates were analyzed to confirm the step change was small enough to justify the assumptions of first order surface reaction kinetics (Fig. S9). The normalized conductivity as a function of time was fitted to a solution of the first order surface oxygen exchange reaction equation using the Matlab program, and the surface exchange coefficient ($k_{s.}$) was obtained.

Computational details

Density functional theory (DFT) calculations were performed using the Vienna *Ab initio* Simulation Package (VASP).[1-3] The Perdew-Burke-Ernzerhof (PBE) functional based on the generalized gradient approximation (GGA) was employed for the total energy calculations.[4] All calculations were expanded using plane-waves up to a cutoff of 400 eV and included spin-polarization. The DFT+U approach[5] was considered with $U_{\text{eff}} = 4.5$ eV (Ti)[6,7], 4.0 eV (Fe)[8] to avoid self-interaction errors in the standard DFT-GGA for strongly correlated electronic materials.[9]

In this study, several types of energetics were calculated to evaluate the properties related to Sr-excess behavior. First, the formation energy of a partial Schottky defect pair ($V_{Sr}^{''}+V_{O}^{\cdot\cdot}$), which is well known to be a favorable point defect in $SrTiO_3$ perovskite,[10,11] was calculated using an STF slab model. Dipole corrections in the *z*-direction were applied to cancel out any errors that may be induced by the asymmetric slabs.[12] A Monkhorst-Pack grid of 4 × 4 × 1 *k*-points was used[13] for (2 × 2) surface unit cells with two constrained bottom layers. Since AO dominated surfaces have been recently observed under SOFC operating conditions in various perovskite oxides,[14-17] the asymmetric SrO-terminated slab model cleaved along the (001) plane was chosen. The slab model contained a ~15 Å vacuum and eight atomic layers. Using this slab model, the partial Schottky formation energy was calculated using the equation below:

$$E_{Schottky}(eV) = E_{SrO\,+\,slab}^{defect} - (E_{slab}^{perfect} + {}^{3}/_{4}E_{SrO\;bulk})$$

where $E_{Schottky}$ is the energy required to form a SrO monolayer on the surface by removing a pair of Sr-O atoms while also generating a $(V_{Sr}^{''} + V_{O}^{\cdot\cdot})$ pair. Here, the formation of strontium-oxide (SrO) was assumed because it is one of the major product phases that results from Sr enrichment. $E_{SrO\,+\,slab}^{defect}$ is the total energy of the slab model with a SrO phase on the topmost layer and the partial Schottky defect in the bulk layer (Fig. S7b). The vacancies of Sr and oxygen are placed at the nearest-neighbor sites. $E_{slab}^{perfect}$ is the total energy of the slab model (Fig. S7a), and $E_{SrO\;bulk}$ is the total energy of bulk SrO containing two Sr and two O atoms. Using our definition, the higher Schottky formation energy indicates the lower extent of Sr enrichment.

Second, the formation energy of STO perovskite ($E_{\mathrm{STO,form}}$) per primitive unit cell and the vacancy formation energies of its constituent elements ($E_{\mathrm{X,vac}}$) were obtained to assess the Sr-O bond strength in a perovskite lattice using the following two equations:

$$E_{STO,form}(eV) = (E_{STO,bulk}^{bare} - \sum_{X} c_X \times E_X)/27$$

and

$$E_{X,vac}(eV) = \left(E_{STO,bulk}^{X,vac} + E_X\right) - E_{STO,bulk}^{bare},$$

where $E_{STO,bulk}^{bare}$ and $E_{STO,bulk}^{X,vac}$ are the total energies of bulk STO perovskite with no defects and an X vacancy (X = Sr, Ti, and O), respectively, and E_X corresponds to the reference energy of the X atom. E_{Sr} and E_{Ti} were obtained from fitted elemental-phase reference energies for accurate estimation of the formation energy.[18] E_O was calculated as half of the total energy of

O_2 in the gas phase. c_X is the number of atoms for each element in the stoichiometric STO perovskite. The (3 × 3 × 3) supercell and a Monkhorst-Pack grid of 3 × 3 × 3 *k*-points were used to describe the bulk STO perovskite.[13] In this study, we observed Sr-excess for STF. However, to elucidate the origin of the change in Sr enrichment upon the applied strain, we used STO bulk to demonstrate that our key claim that Sr atoms are intrinsically under a local compressive state would be generally acceptable for numerous types of STO-based perovskites. In addition, by using the STO bulk model instead of STF, the complexity of arrangements at the B-site caused by Fe doping can be eliminated. To validate this approach, we additionally calculated $E_{\mathrm{STF,form}}$ and $E_{\mathrm{Sr,vac}}$ as functions of the strain in the (3×3×3) $SrTi_{0.52}Fe_{0.48}O_3$ (STF48) bulk structure. Since it is not possible to construct an STF bulk structure with the exact composition of 50% in (3×3×3) supercell, we used the STF48 model with an Fe concentration of 48%, which is as close to 50% as possible (Fig. S5a). In general, a periodically ordered arrangement is used in the perovskite system among the multiple possible structural configurations to reduce artificial anisotropy[19-21]. However, the symmetrical bulk model cannot be constructed in our periodic (3×3×3) supercell model. We thus arranged the Fe and Ti as uniformly as possible. It seems that $E_{\mathrm{Sr,vac}}$ can be affected by the different configurations of the surrounding B-site cations (Ti or Fe), but the effect would not be significant because Sr atoms primarily form the bonds with nearby oxygen atoms. Fig. S5b shows that $E_{\mathrm{Sr,vac}}$ increases up to a certain tensile strain (~ 1.5%) in STF48 bulk, similar to STO bulk (Fig. 4b). This indicates that the stability of the Sr atoms from 0.0% to 1.5% improves even though the overall stability of STF48 perovskite decreases. This result clearly demonstrates that Sr atoms are under a compressive state in STF as well as STO, where the intrinsic instability of the Sr atoms in a perovskite lattice is observed. However, to reduce the complexity and artificiality of the STF bulk model, we believe it is more intuitive to use the

STO bulk model to analyze our experimental observations, as: Sr enrichment is more suppressed in the tensile-strained STF thin films.

To investigate the effect of the Sr-O bond length (strength) on the surface Sr-excess, we calculated the Sr-O bond length by averaging all twelve Sr-O bond lengths in the STO bulk because the Sr vacancy formation energy is determined by the average bond strength (or length) between a Sr atom and the surrounding twelve O atoms. When a cubic STO perovskite is strained along the *x* and *y* directions, the equivalent twelve Sr-O bonds are differentiated into two types where a Sr atom is connected to the oxygen atoms in the SrO layer (bond A) and in the TiO_2 layer (bond B), as shown in Fig. S6a. Therefore, all Sr-O bond lengths are no longer equivalent under the applied strain. In spite of this, the two types of bond lengths nonetheless increase when applying biaxial tensile strain (Fig. S6b), which implies that all Sr-O bonds can be fortified by tensile strain.

In order to prove this, we analytically calculated the lengths of bond A and B as a function of the biaxial strain using the Poisson ratio. The biaxial tensile strain increases the in-plane lattice constant a (Å) but decreases the out-of-plane lattice constant c (Å) according to the Poisson ratio of STO. Consequently, bond A, of $(a/2)\sqrt{2}$ (Å), is undoubtedly stretched in the tensile state due to the increased value of a (Fig. S6b). Although c is reduced somewhat by the tensile strain, elongation of the bond length is also observed in bond B of $\sqrt{a^2 + c^2}/2$ (Å) (red line in Fig. S6b). This is attributed to the fact that the increase in a is always much larger than the decrease in c in STO perovskite with a Poisson ratio of 0.232. Considering that the Poisson ratios for solid materials such as metals and oxides range from 0.1 to 0.3 in most cases[22], this tendency would also be observed in other cubic perovskites (Fig. S6b).

Finally, the formation energy of strontium-oxide (SrO), which is one of the major product phases caused by Sr-excess,[23-26] was introduced to describe Sr enrichment and is calculated by

$$E_{SrO,form}(eV) = E_{SrO + slab}^{perfect} - E_{slab}^{perfect} - E_{SrO\ bulk},$$

where $E_{SrO,form}(eV)$ is the energy required to create a strontium-oxide monolayer on the top surface layer, $E_{SrO + slab}^{perfect}$ and $E_{slab}^{perfect}$ are the total energies of the slab models with/without the SrO phase on the top layer (Fig. S7c and Fig. S7a), respectively, and $E_{SrO\ bulk}$ is the total energy of bulk SrO. The more $E_{SrO,form}$ increases, the more difficult it is to form SrO.

Supplementary References

1. G. Kresse and J. Furthmüller, *Phys. Rev. B*, 1996, **54**, 11169-11186.
2. G. Kresse and J. Furthmüller, *Comp. Mater. Sci.*, 1996, **6**, 15-50.
3. D. S. Sholl and J. A. Steckel, *Density Functional Theory: A Practical Introduction*, John Wiley & Sons, Inc., USA, New Jersey, 2009.
4. J. P. Perdew, K. Burke and M. Ernzerhof, *Phys. Rev. Lett.*, 1996, **77**, 3865-3868.
5. S. L. Dudarev, G. A. Botton, S. Y. Savrasov, C. J. Humphreys and A. P. Sutton, *Phys. Rev. B*, 1998, **57**, 1505-1509.
6. X. Hao, Z. Wang, M. Schmid, U. Diebold and C. Franchini, *Phys. Rev. B*, 2015, **91**, 085204.
7. M. Nolan, *Chem. Commun.*, 2011, **47**, 8617-8619.
8. L. Wang, T. Maxisch and G. Ceder, *Phys. Rev. B*, 2006, **73**, 195107.
9. E. A. Carter, *Science*, 2008, **321**, 800-803.
10. M. J. Akhtar, Z. U. N. Akhtar, R. A. Jackson, and C. R. A. Catlow, *J. Am. Ceram. Soc.*, 2012, **78**, 421-428.
11. T. Tanaka, K. Matsunaga, Y. Ikuhara, and T. Yamamoto, *Phys. Rev. B*, 2003, **68**, 205213.
12. G. Makov and M. C. Payne, *Phys. Rev. B*, 1995, **51**, 4014-4022.

13. H. J. Monkhorst and J. D. Pack, *Phys. Rev. B*, 1976, **13**, 5188-5192.

14. J. Druce, T. Ishihara and J. A. Kilner, *Solid State Ionics*, 2014, **262**, 893-896.

15. J. Druce, H. Téllez, M. Burriel, M. D. Sharp, L. J. Fawcett, S. N. Cook, D. S. MacPhail, T. Ishihara, H. H. Brongersma and J. A. Kilner, *Energy Environ. Sci.*, 2014, **7**, 3593-3599.

16. H. Téllez, J. Druce, Y-W. Ju, J. A. Kilner and T. Ishihara, *Int. J. Hydrogen Energ.,* 2014, **39**, 20856-20863.

17. A. Staykov, H. Téllez, T. Akbay, J. Druce, T. Ishihara and J. Kilner *Chem. Mater.,* 2015, **27**, 8273-8281.

18. V. Stevanović, S. Lany, X. Zhang and A. Zunger, *Phys. Rev. B*, 2012, **85**, 115104.

19. Y. A. Mastrikov, M. M. Kuklja, E. A. Kotomin, and J. Maier, *Energy Environ. Sci.*, 2010, **3**, 1544-1550.

20. Y. A. Mastrikov, R. Kerkle, E. A. Kotomin, M. M. Kuklja, and J. Maier, *Phys. Chem. Chem. Phys.*, 2013, **15**, 911-918.

21. R. Kerkle, Y. A. Mastrikov, E. A. Kotomin, M. M. Kuklja, J. Maier, *J. Electrochem. Soc.*, 2012, **159**, B219-B226.

22. C. Huang and L. Chen, *Adv. Mater.*, 2016, **28**, 8079-8096.

23. Z. Cai, M. Kubicek, J. Fleig and B. Yildiz, *Chem. Mater.,* 2012, **24**, 1116-1127.

24. Y. Chen, W. Jung, Z. Cai, J. J. Kim, H. L. Tuller and B. Yildiz, *Energy Environ. Sci.*, 2012, **5**, 7979-7988.

25. W. Wang and S. P. Jiang, *Solid State Ionics,* 2006, **177**, 1361-1369.

26. S. P. Jiang, *J. Solid State Electrochem.,* 2007, **11**, 93-102.